

Zonated Quantification of Steatosis in an Entire Mouse Liver[☆]

Lars Ole Schwen^{a,*}, André Homeyer^a, Michael Schwier^{a,b}, Uta Dahmen^c, Olaf Dirsch^d, Arne Schenk^{e,f},
Lars Kuepfer^{e,g}, Tobias Preusser^{a,b}, Andrea Schenk^a

^aFraunhofer MEVIS, Universitätsallee 29, 28359 Bremen, Germany

^bJacobs University, Campus Ring 1, 28759 Bremen, Germany

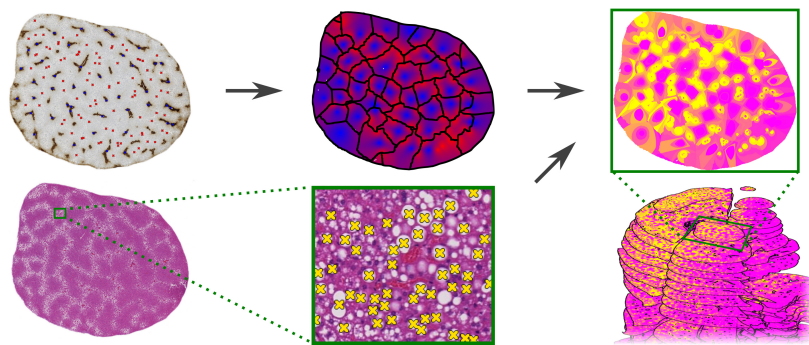
^cExperimental Transplantation Surgery, Department of General, Visceral and Vascular Surgery, University Hospital Jena, Drackendorfer Str. 1, 07747 Jena, Germany

^dInstitute of Pathology, Klinikum Chemnitz, Flemmingstraße 2, 09116 Chemnitz, Germany

^eComputational Systems Biology, Bayer Technology Services, Kaiser-Wilhelm-Allee 1, 51368 Leverkusen, Germany

^fAachen Institute for Advanced Study in Computational Engineering Sciences, RWTH Aachen University, Schinkelstr. 2, 52062 Aachen, Germany

^gInstitute of Applied Microbiology, RWTH Aachen University, Worringerweg 1, 52074 Aachen, Germany



Abstract

Many physiological processes and pathological conditions in livers are spatially heterogeneous, forming patterns at the lobular length scale or varying across the organ. Steatosis, a common liver disease characterized by lipids accumulating in hepatocytes, exhibits heterogeneity at both these spatial scales. The main goal of the present study was to provide a method for zoned quantification of the steatosis patterns found in an entire mouse liver. As an example application, the results were employed in a pharmacokinetics simulation.

For the analysis, an automatic detection of the lipid vacuoles was used in multiple slides of histological serial sections covering an entire mouse liver. Lobuli were determined semi-automatically and zones were defined within the lobuli. Subsequently, the lipid content of each zone was computed. The steatosis patterns were found to be predominantly periportal, with a notable organ-scale heterogeneity.

The analysis provides a quantitative description of the extent of steatosis in unprecedented detail. The resulting steatosis patterns were successfully used as a perturbation to the liver as part of an exemplary whole-body pharmacokinetics simulation for the antitussive drug dextromethorphan. The zoned quantification is also applicable to other pathological conditions that can be detected in histological images. Besides being a descriptive research tool, this quantification could perspectively complement diagnosis based on visual assessment of histological images.

Keywords: histological serial sections, whole-slide scans, zonation, steatosis, Dextromethorphan, quantitative image analysis, pharmacokinetics simulations, Virtual Liver

Abbreviations

CV central vein, **DXM** dextromethorphan, **EvG** Elastica-van Gieson, **GS** glutamine synthetase, **HE** hematoxylin & eosin, **PF** portal field, **PK** pharmacokinetics

[☆]Preliminary results of this study were presented at the Virtual Physiological Human Conference 2014 (VPH 2014): L. O. Schwen, A. Homeyer, M. Schwier, F. Gremse, A. Schenk, L. Kuepfer, U. Dahmen, O. Dirsch, T. Preusser: *Multiscale Simulation of Zonated Metabolism in Steatotic Livers*, available at <http://seek.virtual-liver.de/presentations/703>.

*Corresponding author

1. Introduction

Many physiological processes and pathological conditions in human and animal livers exhibit spatial heterogeneity. Livers are anatomically structured in lobes [1], the liver tissue is structured in lobuli [1], which are in turn subdivided into zones [2, 3]. Typically, metabolic or clearance processes take place in zoned form [4]. This zonation is mainly due to zoned gene/enzyme expression [5, 6]. The size of the respective periportal or pericentral zone depends on the specific phenomenon. In particular for pathological conditions, the sizes may additionally vary over time, e.g., for necrosis and regeneration after administration of carbon tetrachloride [7]. To allow describing the interaction of physiological processes and pathological states with zonation of different size, the classical geometric notion of lobuli divided in three zones [8] was refined to a larger number of zones in this study. Heterogeneity across the organ may be present as well, mainly due to pathological conditions varying at this coarser length scale, e.g., fibrosis [9, 10], cirrhosis [11], or carcinoma [12, 13].

Zonation of pathological conditions is relevant due to their interaction with various metabolic or clearance processes taking place in zoned form [4]. Quantitative data describing the extent of a pathological condition depending on the zonal position can thus provide data complementary to a diagnosis typically based on visual assessment of histological images. Quantifying additionally the organ-scale heterogeneity can help estimate the impact of the disease on overall organ function. Spatially resolved quantitative data describing a liver disease is indispensable for accurate simulations of physiological processes, e.g., [14, 7, 15].

In the present study, steatosis is considered as one example of a pathological condition which is known to occur in spatially heterogeneous form. Steatosis is a common human liver disease frequently caused by dietary misconduct or alcohol abuse [16]. Steatotic livers are characterized by lipids accumulating in the hepatocytes [17]. Steatosis is most typically located in the pericentral region, but it may also occur in periportal form, see [18] and the references therein. In addition, heterogeneity can also be observed across the whole organ [19]. Both zonation and organ-scale heterogeneity were present in the mouse liver considered in this study, see Fig. 1. The main goal of the present study was to quantify these heterogeneities, in order to allow using the results for a pharmacokinetics (PK) simulation.

Clinical diagnosis of steatosis is based on histological assessment of liver biopsies, representing only a tiny fraction of the whole organ. For this purpose, e.g., hematoxylin & eosin (HE) or oil Red-O staining [20] are used, providing a distinction of micro- and macro-vesicular steatosis as well as a zonation [21]. Clearly,

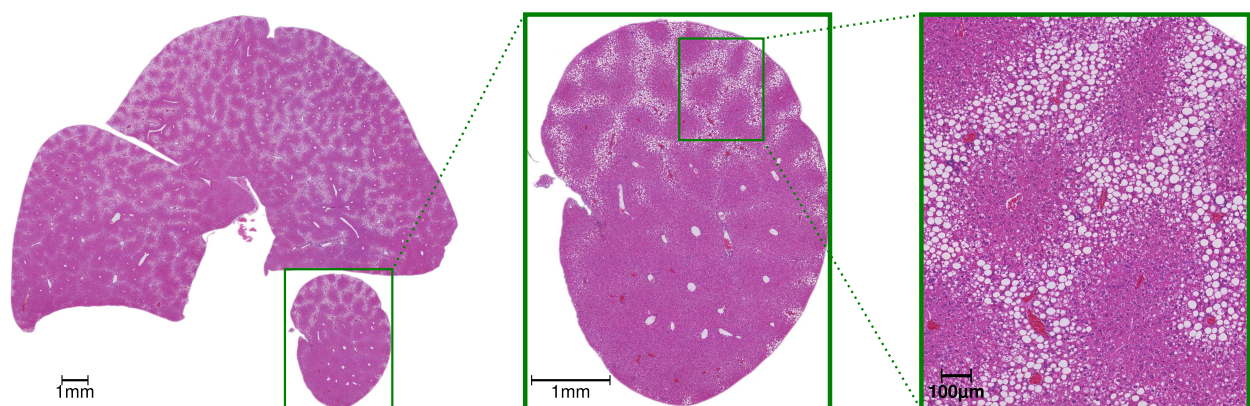


Figure 1: **Heterogeneity of Steatosis.** Large vacuoles in hepatocytes, indicating steatosis, are visible as bright spots in this histological whole-slide scan of a mouse liver shown in three different magnifications (from left to right: whole slide, one lobe, detailed view). The steatosis forms distinct zonal patterns, in this case periportal ones, and occurs spatially heterogeneous across the organ. The main goal of this study was to quantify these heterogeneities.

The images in this figure were manipulated for clarity (removal of background, contrast adjustments).

this only provides local data and does not permit examining the whole organ. Zonation of steatosis is easily assessed qualitatively by experienced pathologists, but is typically not quantified. At the organ scale, steatosis can be quantified using ultrasound and computed tomography [22] as well as magnetic resonance imaging [23], all of which are non-invasive, but do not reveal all features accessible by histology. Experimentally, lipid contents can be determined using biochemical measurements, which can be compared to averaged results obtained by other approaches [24]. This approach, however, lacks spatial resolution.

Detecting lobuli is the basis for zoned quantification. In most species, their boundaries are not determined by anatomical structures, so they need to be inferred from typically optical image data of sufficiently high resolution. A manual approach for determining lobular shapes [25, 26] is of prohibitive workload for more than a few lobuli, so a semi-automatic procedure with an algorithmic component similar to [27] was employed here.

Recent advances in histological whole-slide imaging and image processing [28] permit quantifying steatosis using serial sections of entire organs of small animals such as mice. Besides the detection of lipid vacuoles, steatosis can be quantified as average values per lobe or on smaller tiles, typically squares that are not physiologically motivated. To the best of our knowledge, this kind of analysis has neither previously been performed in 3D to cover a whole organ, nor have zoned distributions and their heterogeneity been quantified at this scale.

Previous own studies [15, 29] showed the influence of spatially resolved pathological perturbations in PK modeling, in particular in combination with zoned metabolism. The present study now offered the opportunity to use actual measured steatosis patterns for the whole organ as opposed to the synthetic spatial patterns used previously [15, 29].

In the present paper, an approach is presented for zoned quantification of steatosis in a mouse liver. For this purpose, histological whole-slide scan images of serial sections of a whole mouse liver with different stainings were used. An image registration was performed for two purposes: for being able to combine information made visible by different stainings [30] and for obtaining 3D analysis results [31]. In our case, portal fields (PFs) and central veins (CVs) were detected using glutamine synthetase (GS) staining in order to determine lobuli and zones within them. In neighboring HE-stained slides, lipid vacuoles indicating macro-vesicular steatosis were detected by an automatic procedure in a set of slides covering an entire liver. This combined analysis was used for zoned quantification of steatosis for the entire liver. Finally, the analysis results were used in a multiscale whole-body PK simulation, in which the liver model represented both organ-scale heterogeneity and zonation.

2. Material and Methods

In this section, the workflow from creating specimens via image registration, annotation of PFs and CVs, tessellation in lobuli and zones, detection of lipid vacuoles, and zoned quantification is presented. The *in silico* part of this workflow is illustrated in Fig. 2. Finally, a modeling approach is described where the analysis result was used as simulation input.

2.1. Histological Imaging of a Steatotic Mouse Liver

Steatosis in a male C57/BL6N mouse (Charles River, Sulzfeld, Germany) was induced by feeding a methionine/choline-deficient high fat diet (E15652-94 EF R/M, high fat MCD mod. low methionine and choline experimental diet [32]; ssniff, Sulzfeld, Germany) for 4 weeks. The animal was sacrificed under anesthesia by exsanguination. The liver was explanted and fixed in 5% buffered formalin followed by paraffin embedding. All procedures and housing of the animals were strictly carried out according to the German animal welfare legislation.

Subsequently, 3 μm sections were prepared using a rotary microtome (Microm HM355S; Thermo Fisher Scientific Microm International GmbH, Walldorf, Germany). In total, a stack of 2037 slides were produced in four batches (1 to 577, 578 to 987, 988 to 1500, and 1501 to 2037). In between each batch, the microtome blade had to be changed and approximately 10 μm of tissue were lost.

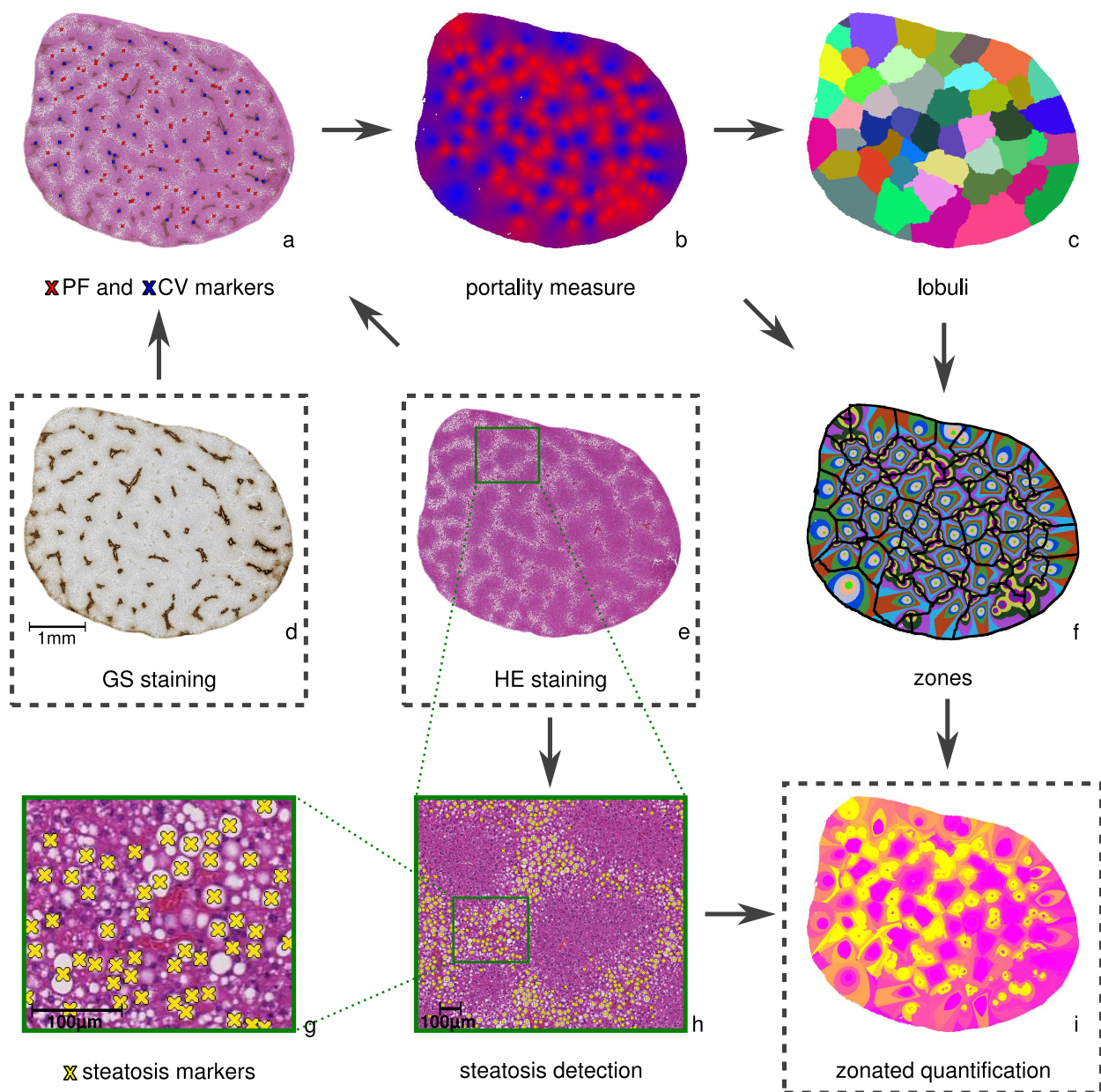


Figure 2: Image Analysis and Quantification Workflow. For one lobe imaged as part of two neighboring registered whole-slide scans, this figure illustrates the image analysis and steatosis quantification workflow. Simultaneously viewing a glutamine synthetase-stained slide (d) and an HE-stained slide (e), portal fields and central veins were annotated manually (a). From these markers, the portality measure (b) as defined in Eq 1 was computed and visualized on a color scale from red (PF) to blue (CV). Lobuli (c) were defined as the catchment basins of a suitably pre-flooded watershed transform (randomized colors, one per lobulus). The portality measure was quantized in $H = 12$ zones, which are visualized (one color per zone) together with lobulus boundaries (black lines) in (f). Macro-vesicular lipid vacuoles were detected automatically in the HE-stained slides as shown in the zoomed views (g, h). Finally, steatosis was quantified as the relative area per zone using an average size of the lipid vacuoles. The results were visualized (i) using a color scale from magenta to yellow (0% to 15% lipid accumulation). Images a, d, e, g, and h were manipulated for clarity (removal of background, contrast adjustments); a is an overlay of d, e and analysis results; g and h were overlaid with analysis results.

The slides were stained in batches of 25 slides. Each batch consisted of a block of 20 slides with Elastica-van Gieson (EvG) and HE staining alternatingly and another block of 5 slides using Gomöri, HE/EvG, Laminin, alpha-smooth muscle actin and GS staining. Finally, the slides were digitalized using a whole-slide scanner (NanoZoomer HT 2.0, Hamamatsu Photonics K. K., Hamamatsu City, Japan; at 400-fold optical magnification) at an in-plane image resolution of 227 nm. Throughout this paper, the term ‘slide’ will be used for both the physical object and the image data of its scan to avoid unnecessary complicated notation. The distinction will be clear from the context.

2.2. Registration of the Histological Images

For registering and analyzing the histological images, the original scans of the slides were downsampled to an in-plane resolution of 908 nm. This resolution was sufficiently fine for detecting features used for registration and for detecting lipid vacuoles, and coarse enough to avoid excessive computational workload.

During the preparation of the histological slides (see Section 2.1) strong rigid deformations occurred when placing a tissue section on a slide. Furthermore, the cutting process inevitably introduced non-linear deformations. Therefore, registration of consecutive histological slides was used for two purposes: First, a geometric matching of lobuli and zones with steatosis was facilitated. To determine lobuli and zones, PFs and CVs needed to be located; they could be distinguished most easily using GS staining. Steatosis was easier to detect in HE staining as the contrast for lipid vacuoles is better than in GS staining. Second, registration also permitted a correct relative alignment within the stack of slides representing the organ.

The registration was performed in several steps. An automatic rigid registration was performed first, it was based on a method described in [33]. This rigid registration was extended to handle several individual tissue sections on one slide by first determining all connected components on both slides to be registered and then determining the best registration matches. However, the rigid registration was not sufficient in all cases. The main causes of error were strong non-linear distortions like tears and cuts, which could not automatically be compensated for. This required a manual review of the slides. In some cases, the distortions could be patched manually and then registered successfully, in other cases, slides had to be discarded. Another cause of error was a wrong correlation of the connected components, which could be easily fixed during the manual review by indicating which components actually corresponded to each other. In about 2% of the cases, the registration failed because the features used for registration were not prominent enough. In those cases, a manual alignment was required.

Since the slides were already aligned fairly well after the previous steps, a fully automatic non-linear registration could be employed as the final step to fix the remaining minor misalignments. The non-linear registration used an elastic regularizer as first introduced by Broit [34] and normalized gradient fields [35, 36] as distance measure, since they proved to be robust towards different stainings.

2.3. Analysis of the Histological Images

In order to cover the whole dataset, the spacing of slides to be analyzed was chosen to be in the range of lobular radii in mice, reported as $284.3 \pm 56.9 \mu\text{m}$ in [37, Table 1]. As some slides were inevitably damaged in the experimental procedure, 34 pairs of neighboring and undamaged GS and HE slides were selected from the 2037 slides used for registration, resulting in a non-equidistant spacing of 150 to 300 μm between the slides to be analyzed.

For obtaining a zoned quantification, the positions of all PFs, CVs, and lipid vacuoles were obtained in the selected HE slides. Macro-vesicular lipid vacuoles were considered to be all lipid vacuoles that are larger than hepatocyte nuclei [38]. The assessment of steatosis was limited to macro-vesicular lipid vacuoles because micro-vesicular steatosis cannot be reliably quantified in HE-stained slides [39].

A particular challenge for the annotation was the large size of histological whole-slide images and the multitude of depicted structures. Therefore, two software tools were developed to facilitate annotation.

The first software tool allowed manual annotation of PFs and CVs. For this purpose, it featured a virtual microscope viewer in which the user could pan and zoom to arbitrary positions in a slide image. PFs and CVs could then be marked by clicking in the image. In HE-stained slides, PFs and CVs were often hard to distinguish. In GS-stained slides, however, both structures could be easily distinguished because

central veins are highlighted in brown. The software tool, therefore, enabled the visual comparison of the current HE slide with the nearest GS slide in the registered tissue volume. The PF and CV annotations were performed by technicians trained in the analysis of histological images.

The second software tool enabled the fully-automatic annotation of the macro-vesicular lipid vacuoles. This tool performed three main processing steps. First, the tissue region within the image was segmented by a tile-based image analysis approached based on [40]. Second, the pixels within the tissue region were classified into background or tissue by thresholds for their brightness and saturation values. Third, blobs of connected background pixels were classified by their shape into either macro-vesicular lipid vacuoles or other background structures, such as vessels or tissue cracks.

The two software tools provided lists of markers (points) for PFs, CVs, and macro-vesicular lipid vacuoles as well as the total area of lipid vacuoles per slide and the ratio of area of lipid vacuoles over area of the entire organ cross section in the slide. The latter implicitly provide the organ cross section in each slide. This data was used for further computations as described next.

2.4. Zonated Quantification of Steatosis

Lobuli in liver tissue are physiologically defined as the regions drained by one CV [1]. The most obvious approach for extracting lobuli from the data would be to tessellate the respective liver mask into the Voronoï cells [41] defined by the CV markers. However, such a Voronoï tessellation ignores the location of the PF inflows and leads to lobulus boundaries not respecting the PF locations. Instead, the following procedure was used: First, a “portality measure” was defined that measures a relative distance to the closest PF and CV points. Quantizing this measure easily resulted in zones. Finally, a preflooded watershed transform of the portality measure allowed defining the respective catchment basins as lobuli, an approach similar to the one used in [27]. A slide-wise 2D procedure is presented here, the extension to 3D is discussed in Section 3.5.

For this study, the division of lobuli in zones was chosen to be such that the distance between PFs and CVs is equidistantly subdivided in $H = 12$ pieces. This choice corresponds to the approximate number of 12.2 ± 2.4 hepatocytes along one lobular radius for mice reported in [37, Table 1]. The structure of the zones matched the PK model in which the analysis data is to be used.

For any point x in the liver,

$$p(x) := 1 - \frac{\text{dist}(x, \text{PF})}{\text{dist}(x, \text{PF}) + \text{dist}(x, \text{CV})} \quad (1)$$

was defined as the portality measure. Clearly, $p(x) = 1$ exactly at the PFs, $p(x) = 0$ at exactly the CVs, and $p(x) \in (0, 1)$ for other points. For a tessellation of the lobuli in H zones, a zone $Z_h, h \in \{0, \dots, H - 1\}$ was defined via the quantization of p as

$$Z_h := \left\{ x : \frac{h}{H} \leq p(x) < \frac{h+1}{H} \right\}. \quad (2)$$

This can easily be adapted if a different motivation of zones is to be considered, e.g., different numbers for other species, a coarser zonation with fewer zones, different numbers of zones corresponding to the size of lobuli.

While the definitions in (1) and (2) are continuous, these values were actually computed on discrete points and separately in each slide. For this purpose, a resolution of $7.264 \mu\text{m}$ was chosen, one eighth of the resolution of the image data used for the previous steps. This was still sufficiently fine compared to the size of liver cells, reported as $23.3 \pm 3.1 \mu\text{m}$ in [37, Table 1] for hepatocytes in mice. Marker positions for PFs, CVs, and lipid vacuoles as well as the areas of lipid vacuoles were unaffected by this resampling. These quantities were determined at the previous resolution of 908 nm .

Next, the preflooded watershed transform [42] of p was computed separately for each slide. The PF locations are maxima of p of equal height and CV locations are minima of p , also of equal height, and ridges of p intuitively correspond to lobulus boundaries. Hence lobuli could be defined to be the catchment

basins obtained from the watershed transform. The preflooding height was chosen per slide so that the number of catchment basins coincided with the number of CV markers. This is not always possible exactly, so a trade-off was chosen between avoiding artificial catchment basins resulting from the image processing and avoiding combined catchment basins for distinct CV locations. Let L denote this total number of lobuli obtained by this analysis.

Finally, the ratio of lipid accumulation $s_{h,l}$ in zone $h \in \{0, \dots, H-1\}$ in lobulus $l \in \{0, \dots, L-1\}$ was computed as

$$s_{h,l} = \frac{(\text{average vacuole size}) \times (\text{number of lipid vacuole markers in zone } h \text{ in lobulus } l)}{\text{total size of zone } h \text{ in lobulus } l} \quad (3)$$

For each slide, the total lipid area was divided by the number of lipid markers to obtain the average size of a lipid vacuole. Both these values were available from the analysis described in Section 2.3. Future work will include refined analysis taking into account the size of individual lipid vacuoles and extend the assessment towards micro-vesicular steatosis. Lipid vacuoles appeared to be larger towards the PFs as shown, e.g., in Fig. 1. There seems to be generally a gradual decrease of the size of lipid vacuoles towards the CVs, without substantial variation in the number of lipid vacuoles per area. This could indicate that the approach used here underestimates the heterogeneity (as it assumes constant size) and the zonation is actually stronger, i.e., higher values of lipid accumulation near the PFs and smaller values towards the CVs. On the other hand, microvesicular steatosis not included in the analysis could lead to slightly larger values lipid accumulation towards the CVs. A future refined analysis will permit quantifying this effect and permit an investigation of the zonal distribution of sizes.

Depending on later applications, a clustering of lobuli with ‘similar’ steatosis patterns and the corresponding cumulative volumes may be useful. One possible clustering approach is presented in Section 2.5 as an example. It is rather generic, but nonetheless suitable for the purpose at hand.

2.5. Pharmacokinetics Modeling in Steatotic Livers

The steatosis analysis results were used for a PK simulation of the clearance of dextromethorphan (DXM) in mice. This antitussive drug is widely used in humans [43] and was chosen for this application due to its high lipophilicity of $\log P = 3.2$. In mouse livers, it is metabolized pericentrally and thus provides interesting interactions with the predominantly pericentral steatosis profiles. More precisely, DXM is metabolized by the enzyme Cyp2d22 in mice [44]. This enzyme is expressed in approximately the pericentral half of the lobular area (own estimate based on the immunohistochemical image shown in [45, Fig. 9]).

For the simulations presented here, a multi-scale perfusion and PK simulation framework [29] was used with parameters from an existing physiologically based PK model for DXM in mice [46], exported from the software PK-Sim[®] [47]. In summary, the multiscale model [29] extends an established whole-body PK model [47], mainly in two aspects. A recirculation delay is present for more accurate temporal resolution, and a spatio-temporally model for the liver is used. In the latter, one-dimensional representative sinusoids divided in 12 zones are employed for reflecting zonation of metabolic properties such as the presence of Cyp enzymes and pathological model perturbations such as steatosis. Organ-scale heterogeneity is reflected by considering multiple representative sinusoids in parallel, e.g., one for each lobulus. For each zone h in each representative sinusoid l , the amount $s_{h,l}$ of lipid accumulation due to steatosis from (3) was specified. It influences the model parameters via the respective intracellular partition coefficients, in the same simplified manner as previously considered in [15]. For the dataset considered here, no geometric models for the vascular trees were available that could be used as optional input for the multiscale model. Instead, a fixed delay between liver inflow and PFs as well as between CVs and liver outflow of 2s each was assumed.

In this setting, a single representative sinusoid could be used to reflect multiple lobuli with essentially the same steatosis pattern. For this purpose, a simple 12-dimensional clustering strategy was employed. The components of $s_{h,l}$ for lobulus l were quantized to multiples of a chosen quantization parameter, thus binning the steatosis patterns. An average of the original steatosis patterns was computed for each bin,

weighted by the respective sizes of the detected lobuli. Additionally, bins with a total size below a given threshold were omitted from the simulation. The quantization parameter was heuristically chosen to be 0.08 and the threshold as $5 \cdot 10^{-4}$ times the total size. Developing a more refined clustering strategy is future work, taking into account the sensitivity of the simulation results to the steatosis data as well as an estimate of the error introduced by the image processing and quantification procedure.

3. Results and Discussion

3.1. Lobulus Tessellation

From the annotation of PFs and CVs, total numbers of exactly 13000 PF markers and 11534 CV markers were obtained. A total number of 11504 lobuli is obtained from (2) by the procedure described in Section 2.5. Hence, the trade-off for choices of preflooding heights in the watershed transform resulted in only 30 or 0.26 % of CV markers not assigned a separate catchment basin (lobulus). This number of lobuli was larger than a previous own estimate of 6281 lobuli in a mouse liver [48] based on the respective sizes. The present approach probably overestimated the number of lobuli due to the fact that one lobulus may be part of more than one of the slides considered for the analysis. In particular, the slides intersected many lobuli peripherally. The mean \pm standard deviation of the sizes were $0.281 \pm 0.157 \text{ mm}^2$. This shows that the sizes determined in the 2D slides here generally agreed with literature values, e.g., the size of $0.21 \pm 0.05 \text{ mm}^2$ in mice reported in [37, Table 1]. Fig. 3 shows more detailed plots of these values. In the boxplot, whisker lengths correspond to 1.5 times the interquartile range. Besides the aforementioned effect of peripherally intersected, i.e., unrealistically small lobuli, there are also outliers of unrealistically large lobuli, most likely due to poorly visible CVs missed in the annotation, despite the GS staining. Additionally, [37] was focused on lobuli intersected transversely, whereas the present analysis considers lobuli intersected in any orientation.

3.2. Steatosis Analysis

The automatic detection of lipid vacuoles resulted in a total number of 529633 markers. The results were verified by visual inspection and had the accuracy to be expected, 92 %, for the method employed [49].

The average size of the lipid vacuoles was determined for each slide as total lipid area divided by the number of lipid vacuole markers as needed for (3). This average varied substantially between different slides as shown in Fig. 4, mean \pm standard deviation was $135.5 \pm 28.2 \mu\text{m}^2$. A density of lipid vacuoles was determined for each slide as the number of lipid vacuole markers divided by the total cross section area of the organ in the respective slide. This density also varied substantially between different slides, cf. Fig. 5, mean \pm standard deviation was 182.97 ± 188.52 per mm^2 . In both cases, the data does not seem to follow a normal distribution, so the standard deviations should be interpreted with caution. Together, these variations indicate an organ-scale heterogeneity of steatosis not only in terms of the number of lipid

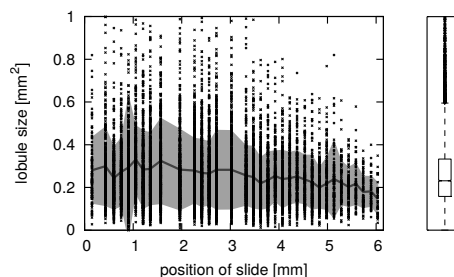


Figure 3: **Lobulus Sizes.** The plot shows the variation of the lobulus sizes as obtained by the described tessellation procedure. Sizes were plotted against the position of the respective slide in the stack, where 0 mm corresponds to the top of the stack visualized in Fig. 6. This indicates that there was no systematic variation in detected lobulus sizes in stacking direction. The box-and-whisker plot on the *right* additionally shows the distribution of the sizes without taking into account the position.

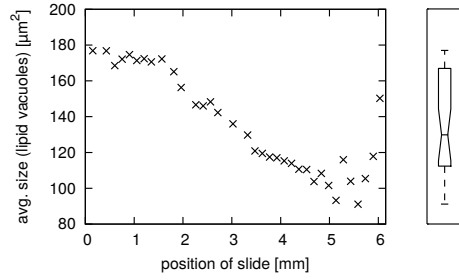


Figure 4: **Average Size of Lipid Vacuoles.** The plot shows the variation of the average sizes of lipid vacuoles per slide as needed for zoned quantification of steatosis. These average sizes were plotted against the position of the respective slide in the stack, where 0 mm corresponds to the top of the specimen visualized in Fig. 6. The plot indicates a clear trend of decreasing average size from one side of the stack to the other, except for variations in the last slides with comparably small tissue intersections. The box-and-whisker plot on the *right* additionally shows the distribution of the average sizes of the lipid vacuoles without taking into account the position.

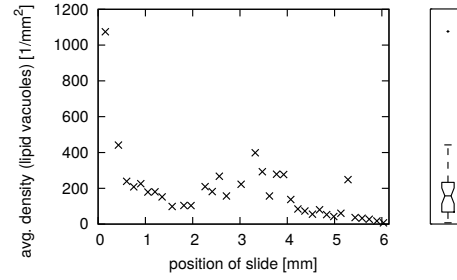


Figure 5: **Average Density of Lipid Vacuoles.** The plot shows the variation of the average number of lipid vacuoles per area of the organ cross section for each slide. These densities were plotted against the position of the respective slide in the stack, where 0 mm corresponds to the top of the specimen visualized in Fig. 6. This plot indicates a strong variation of the density of lipid vacuoles across the specimen with only a weak trend of decreasing density from top to bottom. The box-and-whisker plot on the *right* additionally shows the distribution of the density of lipid vacuoles without taking into account the position.

vacuoles, but also in terms of their size. This probably has an impact on the analysis results in the slides also exhibiting organ-scale heterogeneity and will be investigated in more detail using a further refined analysis procedure in the future.

3.3. Zonated Quantification

The results of the zonated quantification of steatosis are visualized in Fig. 6 for the full stack of slides considered. This figure indicates an organ-scale decrease of lipid fractions from one side of the stack to the other. The distributions of lipid fractions along the $H = 12$ zones for all 11 504 lobuli detected in the dataset are shown in Fig. 7, clearly confirming the predominantly periportal patterns of the steatosis already visible in the HE slides. Moreover, these plots show the reduction from 11 504 to 105 substantially different steatosis patterns by the binning described in Section 2.5.

The organ-scale heterogeneity was further investigated in terms of the lipid content $s_{1,l}, \{0, \dots, L - 1\}$ in the second zone, where the peak of the average lipid content per zone occurs (see Fig. 7). The $s_{1,l}$ are plotted in Fig. 8 depending on the position of the respective slide in the stack, showing a clear decrease of the $s_{1,l}$ from one side of the stack to the other. This confirms the observation of an organ-scale heterogeneity in Fig. 6.

3.4. Pharmacokinetics Simulation

As explained in Section 2.5, a clustering approach was used to obtain 105 substantially different steatosis patterns from the full analysis. Along with the respective cumulative volumes, this data was used in a model with 105 representative sinusoids with different steatosis patterns for performing a whole-body PK simulation involving DXM. For this purpose, an infusion of 5 mg per kg body weight [46] into the portal vein, lasting for 10 seconds, was simulated. This is certainly an unphysiological scenario for a drug typically administered orally, but was chosen to avoid complicating the example application by a model for oral uptake. For comparison to a healthy liver, an additional simulation considering a single representative sinusoid for the whole liver without steatotic lipid accumulations was considered, using the same infusion profile as before. These simulations were run for 180 minutes.

The systemic DXM concentrations in the venous blood pool are shown in Fig. 9. According to the PK model, the DXM was mostly taken up by the liver during the first pass and was released slowly afterwards, while at the same time being cleared from the model organism. The impact of steatosis at the systemic level (Fig. 9) can be observed mainly during the first 10 minutes of the simulation. After that, the difference

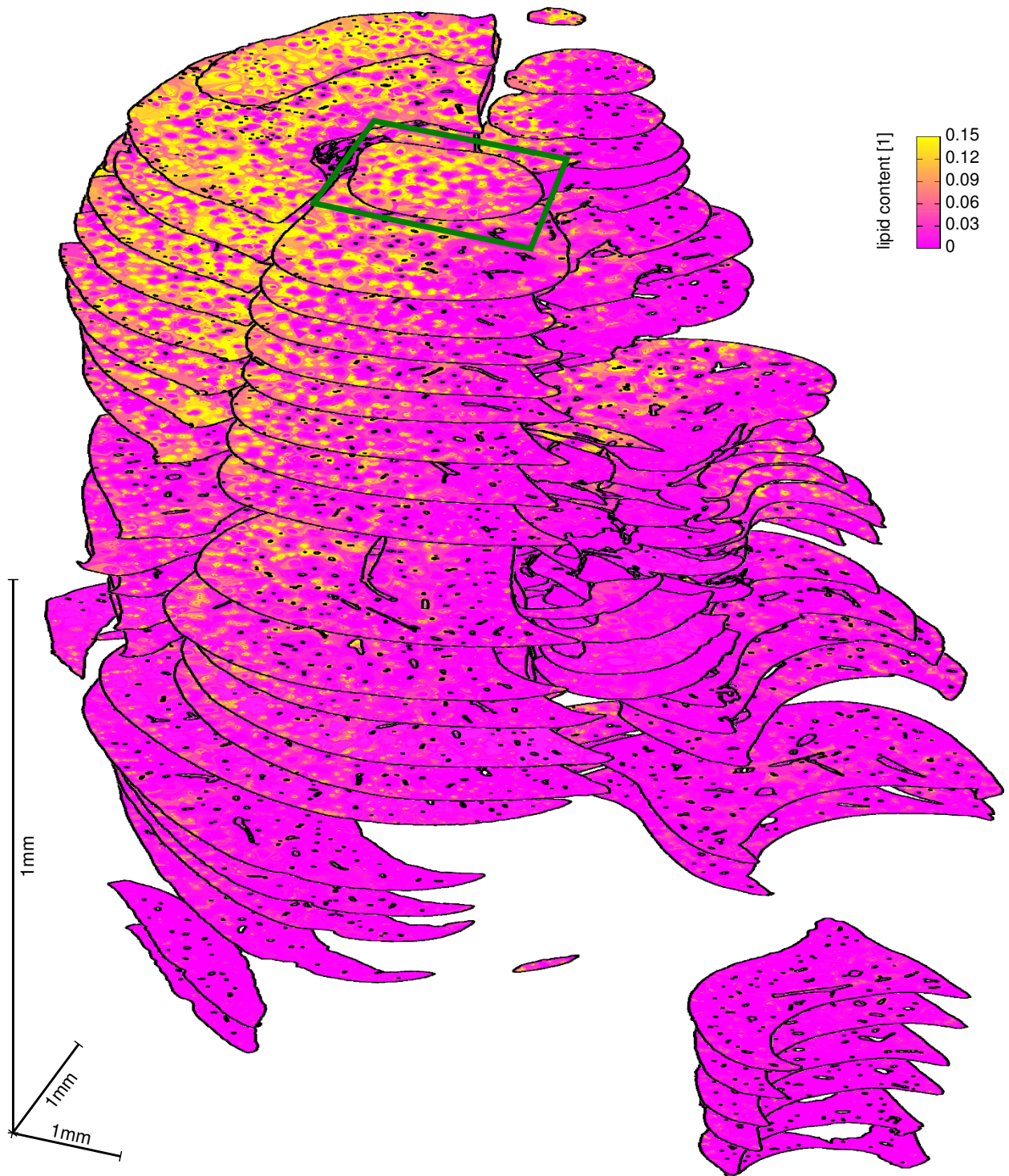


Figure 6: **Organ-Scale Zonated Quantification of Steatosis.** The analysis illustrated in Fig. 2 was applied to 34 whole-slide scans covering a whole mouse liver in a non-equidistant manner. Results were visualized per slide on a color scale from magenta to yellow, the inter-slide spacing was stretched to enhance the visualization. The green box highlights the lobe in one slide shown in more detail in Fig. 2.

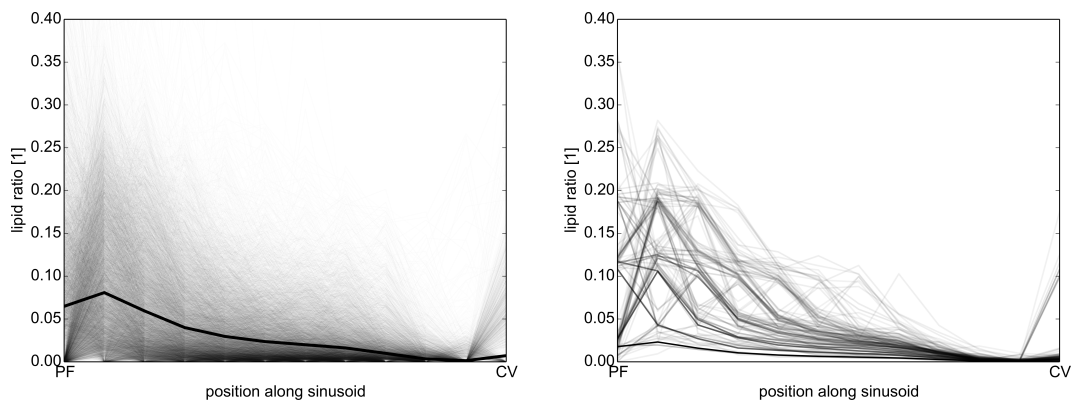


Figure 7: **Steatosis Zonation Patterns.** The (*left*) plot shows the distribution of steatosis zonation patterns for all 11 504 detected lobuli. The thick line in the left plot indicates the average lipid ratio per zone, obtained by weighting by the respective lobulus size, whereas the volumes corresponding to the patterns are indicated by the opacity of the respective lines. This confirms the predominantly periportal accumulation of lipid vacuoles qualitatively visible in Fig. 1, 2, and 6. Applying a clustering of similar steatosis patterns resulted in 105 patterns shown in the *right* plot.

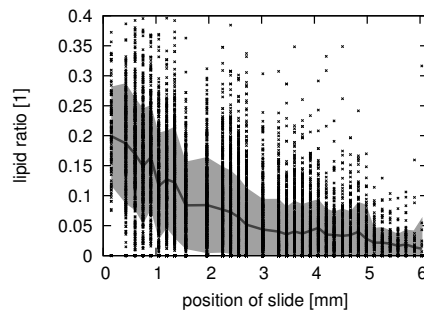


Figure 8: **Lipid Contents in Second Zone.** The plot shows the lipid ratios for the second zone in all 11 504 lobuli, plotted against the position of the respective slide where 0mm corresponds to the top of the stack visualized in Fig. 6. The second zone is where, on average, the highest lipid ratio was attained, see Fig. 7. The thick line and the shaded region show the (unweighted) average and the standard deviation for each position, respectively. The plot shows a clear trend indicating an organ-scale decrease of lipid accumulation from one side to the other.

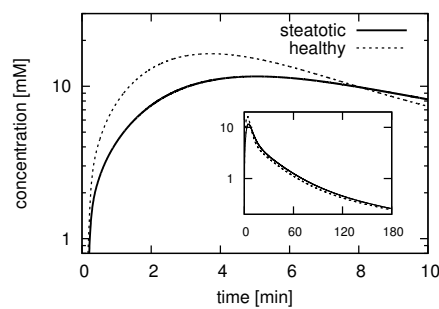


Figure 9: **Systemic Dextromethorphan (DXM) Concentration.** The plot shows the simulated DXM concentrations in the venous blood pool of the model organism. Curves are shown for the steatotic liver as quantified in this study and, for qualitative comparison, for a healthy liver. The difference can mainly be observed for the first 10 minutes of the simulation (*large plot*) and becomes less prominent after that (*inset*).

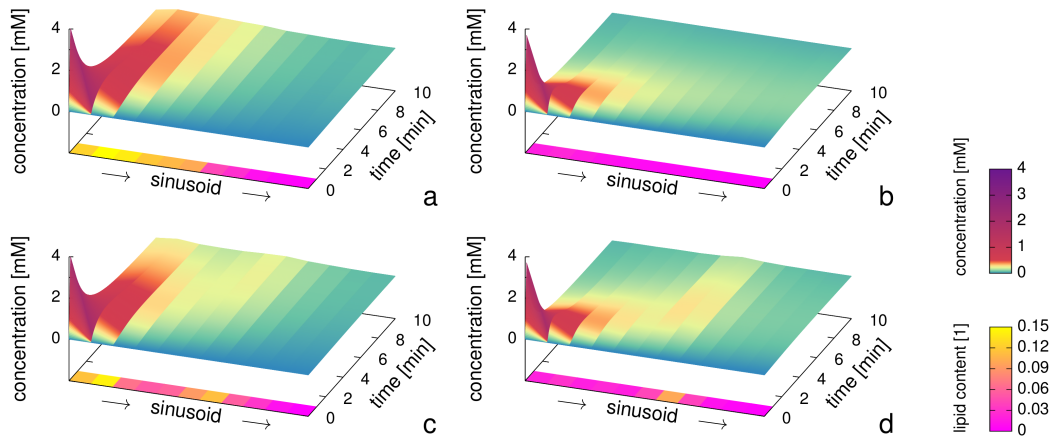


Figure 10: **Spatio-Temporal Concentration Profiles.** The plots show spatio-temporal distribution of dextromethorphan (DXM) in the cells along representative sinusoids used in the pharmacokinetics simulations. More precisely, the influence of the underlying steatosis pattern on the DXM distribution is illustrated. Four different steatosis patterns were chosen for this plot, one predominantly periportal lipid accumulations (a), one case with negligible steatosis (b), and two less typical patterns in the specimen (c, d). Due to its lipophilicity, DXM was retained by steatotic cells longer than by non-steatotic cells and the peak propagated more slowly across steatotic regions.

between healthy and steatotic case becomes less pronounced, but is nonetheless visible in the simulation output.

More detailed spatio-temporal concentration profiles for four representative sinusoids with different steatosis patterns are shown in Fig. 10 for the first 10 minutes of the simulation. The plots show how a higher lipid content in the cells leads to a higher uptake of the lipophilic substance DXM in the cells.

3.5. Perspective

The results presented in Figures 3, 4, 5, 6, and 8 are three-dimensional results of analyses separately performed in two dimensions. They could, on the one hand, immediately be refined by a more dense use of GS staining within the serial sections. In this case, more slides can be used for PF and CV detection and thus provide more lobulus data, and more neighboring HE slides can be used for steatosis detection. On the other hand, the analysis techniques presented here can be extended to a fully 3D zoned analysis. For this purpose, portality can be defined based on distances to the centerlines of the PFs and CVs rather than point markers. The watershed transform needs to be computed in 3D after choosing a suitable global preflooding, and the term ‘size’ in (3) needs to be interpreted as volume. Besides creating a potentially larger computational workload, the quantification can thus be transferred to 3D. In 3D, the quantification could benefit from tracking the vascular structures for distinguishing more easily between PFs and CVs. At the same time, this could provide the vasculature for subsequent simulations, as used, e.g., in [15, 29], and thus provide the full link between organism and parenchymal scale for multi-scale liver simulations [50, 51].

The computation of lobuli used here relied on PF and CV positions. Besides intra-observer variability in the manual annotation, this involved potential sources of errors also relevant for future automatic detection. PF positions may have been missed primarily if portal triads could not be distinguished from lipid vacuoles. Clearly, the accumulation of lipid vacuoles could not be used as an indicator for PF positions when investigating whether there is a correlation or not. Missing PF markers resulted in incorrect zones, but this did not have a major influence on the results as a lobulus tessellation rather than an acinus [1] tessellation is considered. CV positions may have been indiscernible even though GS staining is visible in the neighboring slide. Missing CV markers resulted in artificially large lobuli and incorrect zones. Due to the clear visibility of the GS staining, this rarely happened and had only a minor influence on the results. Moreover, tracking PFs and CVs in a future 3D analysis will further reduce PF and CV detection errors.

For a future evaluation and validation of the lipid contents quantified by the technique presented here, a comparison to results obtained by other measurement techniques will be necessary.

Similarly, the PK simulation shown as a proof of concept application needs to be refined and validated before it can be used for predictive purposes. For a detailed discussion of the PK simulation framework used here, in particular the simplified way steatosis is represented in the model, see [29]. Moreover, estimating of Cyp2d22 presence from an image of a single lobulus [45, Fig. 9] from the literature yields only a non-objective and coarse estimate. While this is sufficient for our application, a future, more refined model should be based on more targeted data. For this purpose, the respective relevant enzyme should be stained in the same serial section of a steatotic liver, quantified systematically in more than a single lobulus in merely one slice, and correlated with the extent of steatosis.

The presented, modular approach for zoned quantification is based on marker positions and thus by no means limited to analyzing steatosis. In fact, the steatosis detection can easily be replaced by detection of other phenomena such as proliferation or necrosis [40] in the histological slides based on a staining targeted for the respective phenomenon. Similarly, the number or geometric definition of zones can be changed. This way, the zonation of other phenomena can also be quantified and the data can subsequently be used in the same manner as the steatosis data considered here. To improve PK simulations, enzyme expression profiles relevant for zoned metabolism can be determined in neighboring, appropriately stained slides from the same specimen as used to measure the pathological perturbation.

The quantitative results in Figures 4, 5, and 8 indicate an organ scale heterogeneity of the extent of steatosis. The apparent trend depending on the slice position in the specimen. In order to correlate this heterogeneity with anatomical structures, the presented analysis methods will be extended in the future, e.g., so that different liver lobes can be separated in the slides and analyzed separately in 3D. This will permit anatomically motivated investigations of variations between or within lobes, e.g., differences between the interior and regions near the boundary.

For the analysis results presented here, a single organ at a single time point for a specific way of inducing steatosis was considered, so the analysis results obtained so far should be viewed as one example snapshot. The methodology, however, permits a comparison of steatosis patterns not only within one organ, but clearly also between different individuals. It is known that total hepatic lipid content differs between individuals under similar conditions, see, e.g., [24]. A zoned quantification could show whether these differences are due to essentially the same zonation patterns of different intensity, or whether there are also substantial differences between the zonation patterns. The zoned analysis thus provides a research tool to quantify how steatosis patterns differ, e.g., between different individuals, over time, or between steatosis occurring due to different causes, and hence support respective future investigations.

The presented methodology for zoned quantification can also be applied to serial sections of smaller tissue samples not covering an entire liver. The analysis is thus also applicable in cases where creating, staining, and scanning serial sections of a whole liver would mean a prohibitive effort, or for clinical applications where explantation of the entire liver is clearly infeasible. In this case, organ-scale heterogeneity is limited to what is sampled by one or more biopsies. Zoned quantification of steatosis or other phenomena in biopsies can thus complement a visual assessment of the individual slides. If future investigations show that different zoned patterns can be used to characterize different states of diseases, the zoned quantification can perspective provide valuable additional information for diagnosis.

4. Conclusion

Registering and analyzing slides of histological serial sections of a mouse liver permits detecting lobuli, defining zones, and zoned quantification of pathological states. For the first time, this analysis was performed to detect steatosis throughout a whole mouse liver, providing a quantification of zonation patterns as well as a notable organ-scale heterogeneity. The analysis result was successfully used as a spatially resolved perturbation to the liver in an exemplary whole-body PK simulation. Combined with future detection of other phenomena in histological images, zoned quantification is a powerful research tool. It can provide biological insights as well as input data for spatially resolved simulations of physiological processes.

Acknowledgements

The authors would like to thank Stephanie Lange and Kathrin Schulze for animal care as well as for preparing, staining, and scanning the serial sections; Christiane Engel and Andrea Koller for annotating PFs and CVs in the histological images; Stefan Höhme for fruitful discussions about lobular subdivision; and Christian Schumann for valuable suggestions regarding 3D visualization.

This work was funded by the German Federal Ministry of Education and Research (BMBF) as part of the systems biology network Virtual Liver (<http://www.virtual-liver.de/>), grant numbers 0315747 (ArS, LK), 0315765 (OD, UD), and 0315769 (AH, AnS, LOS, MS, TP). The funding agency was not involved in study design, collection/analysis/interpretation of data, writing the report, and decision to submit the article for publication.

Author Contributions

UD and OD performed the experiments (experimental design, induction of steatosis, generation and processing of samples: cutting, staining, and scanning the histological serial sections). MS implemented and performed the image registration. AH developed the software for the image annotation and steatosis detection. LOS implemented and performed zoned quantification as well as the pharmacokinetics simulations. ArS and LK provided and adapted the pharmacokinetics model. All authors participated in writing the manuscript and approved the final article.

References

- [1] E. Kuntz, H.-D. Kuntz, *Hepatology: Textbook and atlas*, 3rd Edition, Springer, Heidelberg, 2008.
- [2] D. L. Miller, C. S. Zanolli, J. J. Gumucio, Quantitative morphology of the sinusoids of the hepatic acinus, *Gastroenterology* 76 (5) (1979) 965–969. doi:10.1016/S0016-5085(79)91326-X.
- [3] D. E. Kleiner, E. M. Brunt, Nonalcoholic fatty liver disease: pathologic patterns and biopsy evaluation in clinical research, *Seminars in Liver Disease* 32 (1) (2012) 3–13. doi:10.1055/s-0032-1306421.
- [4] R. Gebhardt, Metabolic zonation of the liver: regulation and implications for liver function, *Pharmacology & Therapeutics* 53 (3) (1992) 275–354. doi:10.1016/0163-7258(92)90055-5.
- [5] K. Jungermann, Zonation of metabolism and gene expression in liver, *Histochemistry and Cell Biology* 103 (2) (1995) 81–91. doi:10.1007/BF01454004.
- [6] K. O. Lindros, Zonation of cytochrome P450 expression, drug metabolism and toxicity in liver, *General Pharmacology: The Vascular System* 28 (2) (1997) 191–196. doi:10.1016/S0306-3623(96)00183-8.
- [7] F. Schliess, S. Hoehme, S. G. Henkel, A. Ghallab, D. Driesch, J. Böttger, R. Guthke, M. Pfaff, J. G. Hengstler, R. Gebhardt, D. Häussinger, D. Drasdo, S. Zellmer, Integrated metabolic spatial-temporal model for the prediction of ammonia detoxification during liver damage and regeneration, *Hepatology* 60 (6) (2014) 2040–2051. doi:10.1002/hep.27136.
- [8] A. M. Rappaport, Z. J. Borowy, W. M. Loughheed, W. N. Lotto, Subdivision of hexagonal liver lobules into a structural and functional unit. Role in hepatic physiology and pathology, *The Anatomical Record* 119 (1) (1954) 11–33. doi:10.1002/ar.1091190103.
- [9] P. Bedossa, D. Dargère, V. Paradis, Sampling variability of liver fibrosis in chronic hepatitis C, *Hepatology* 38 (2003) 1449–1457. doi:10.1016/j.hep.2003.09.022.
- [10] N. S. Goldstein, F. Hastah, M. V. Galan, S. C. Gordon, Fibrosis heterogeneity in nonalcoholic steatohepatitis and hepatitis C virus needle core biopsy specimens, *American Journal of Clinical Pathology* 123 (2005) 382–387. doi:10.1309/EY72F1EN9XCB1KXX.
- [11] B. Maharaj, W. P. Leary, A. D. Naran, R. J. Maharaj, R. M. Cooppan, D. Pirie, D. J. Pudifin, Sampling variability and its influence on the diagnostic yield of percutaneous needle biopsy of the liver, *The Lancet* 327 (8480) (1986) 523–525. doi:10.1016/S0140-6736(86)90883-4.
- [12] P. Vaupel, F. Kallinowski, P. Okunieff, Blood flow, oxygen and nutrient supply, and metabolic microenvironment of human tumors: a review, *Cancer research* 49 (23) (1989) 6449–6465. URL <http://cancerres.aacrjournals.org/content/49/23/6449>
- [13] M. A. Avila, C. Berasain, L. Torres, A. Martín-Duce, F. J. Corrales, H. Yang, J. Prieto, S. C. Lu, J. Caballería, J. Rodés, J. M. Mato, Reduced mRNA abundance of the main enzymes involved in methionine metabolism in human liver cirrhosis and hepatocellular carcinoma, *Journal of Hepatology* 33 (6) (2000) 907–914. doi:10.1016/S0168-8278(00)80122-1.
- [14] T. Ricken, D. Werner, H.-G. Holzhütter, M. König, U. Dahmen, O. Dirsch, Modeling function–perfusion behavior in liver lobules including tissue, blood, glucose, lactate and glycogen by use of a coupled two-scale PDE–ODE approach, *Biomechanics and Modeling in Mechanobiology* 14 (3) (2015) 515–536. doi:10.1007/s10237-014-0619-z.
- [15] L. O. Schwen, M. Krauss, C. Niederal, F. Gremse, F. Kiessling, A. Schenk, T. Preusser, L. Kuepfer, Spatio-temporal simulation of first pass drug perfusion in the liver, *PLOS Computational Biology* 10 (3) (2014) 1–18, e1003499. doi:10.1371/journal.pcbi.1003499.

- [16] S. Bellentani, G. Saccoccio, F. Masutti, L. S. Crocè, G. Brandi, F. Sasso, G. Cristanini, C. Tiribelli, Prevalence of and risk factors for hepatic steatosis in Northern Italy, *Annals of Internal Medicine* 132 (2) (2000) 112–117. doi:10.7326/0003-4819-132-2-200001180-00004.
- [17] A. Lonardo, S. Lombardini, M. Ricchi, F. Scaglioni, P. Loria, Review article: hepatic steatosis and insulin resistance, *Alimentary Pharmacology & Therapeutics* 22 (s2) (2005) 64–70. doi:10.1111/j.1365-2036.2005.02600.x.
- [18] B. S. Hijmans, A. Grefhorst, M. H. Oosterveer, A. K. Groen, Zonation of glucose and fatty acid metabolism in the liver: Mechanism and metabolic consequences, *Biochimie* 96 (2014) 121–129. doi:10.1016/j.biochi.2013.06.007.
- [19] V. Capitan, J.-M. Petit, S. Aho, P.-H. Lefevre, S. Favelier, R. Loffroy, P. Hillon, D. Krausé, J.-P. Cercueil, B. Guiu, Macroscopic heterogeneity of liver fat: an MR-based study in type-2 diabetic patients, *European Radiology* 22 (10) (2012) 2161–2168. doi:10.1007/s00330-012-2468-4.
- [20] A. P. Levene, H. Kudo, M. J. Armstrong, M. R. Thursz, W. M. Gedroyc, Q. M. Anstee, R. D. Goldin, Quantifying hepatic steatosis – more than meets the eye, *Histopathology* 60 (6) (2012) 971–981. doi:10.1111/j.1365-2559.2012.04193.x.
- [21] S. K. Hourigan, M. Torbenson, E. Tibesar, A. O. Scheimann, The full spectrum of hepatic steatosis in children, *Clinical Pediatrics* 54 (7) (2015) 635–642. doi:10.1177/0009922814566927.
- [22] N. F. Schwenzer, F. Springer, C. Schraml, N. Stefan, J. Machann, F. Schick, Non-invasive assessment and quantification of liver steatosis by ultrasound, computed tomography and magnetic resonance, *Journal of Hepatology* 51 (3) (2009) 433–445. doi:10.1016/j.jhep.2009.05.023.
- [23] I. S. Idilman, H. Aniktar, R. Idilman, G. Kabacam, B. Savas, A. Elhan, A. Celik, K. Bahar, M. Karcaaltincaba, Hepatic steatosis: quantification by proton density fat fraction with MR imaging versus liver biopsy, *Radiology* 267 (3) (2013) 767–775. doi:10.1148/radiol.13121360.
- [24] C. D. G. Hines, H. Yu, A. Shimakawa, C. A. McKenzie, T. F. Warner, J. H. Brittain, S. B. Reeder, Quantification of hepatic steatosis with 3-T MR imaging: validation in ob/ob mice, *Radiology* 254 (1) (2009) 119–128. doi:10.1148/radiol.09090131.
- [25] H. F. Teutsch, D. Schuerfeld, E. Groezinger, Three-dimensional reconstruction of parenchymal units in the liver of the rat, *Hepatology* 29 (1999) 494–505. doi:10.1002/hep.510290243.
- [26] H. F. Teutsch, The modular microarchitecture of human liver, *Hepatology* 42 (2) (2005) 317–325. doi:10.1002/hep.20764.
- [27] A. Friebe, J. Neitsch, T. Johann, S. Hammad, J. G. Hengstler, D. Drasdo, S. Hoehme, TiQuant: Software for tissue analysis, quantification and surface reconstruction, *Bioinformatics* 31 (19) (2015) 3234–3236. doi:10.1093/bioinformatics/btv346.
- [28] J. D. Webster, R. W. Dunstan, Whole-slide imaging and automated image analysis considerations and opportunities in the practice of pathology, *Veterinary Pathology Online* 51 (1) (2014) 211–223. doi:10.1177/0300985813503570.
- [29] L. O. Schwen, A. Schenk, C. Kreutz, J. Timmer, M. M. Bartolomé Rodríguez, L. Küpfer, T. Preusser, Representative sinusoids for hepatic four-scale pharmacokinetics simulations, *PLoS ONE* 10 (7) (2015) e0133653. doi:10.1371/journal.pone.0133653.
- [30] Y. Song, D. Treanor, A. J. Bulpitt, D. R. Magee, 3D reconstruction of multiple stained histology images, *Journal of Pathology Informatics* 4 (Suppl. 5). doi:10.4103/2153-3539.109864.
- [31] N. Roberts, D. Magee, Y. Song, K. Brabazon, M. Shires, D. Crellin, N. M. Orsi, R. Quirke, P. Quirke, D. Treanor, Toward routine use of 3D histopathology as a research tool, *The American Journal of Pathology* 180 (5) (2012) 1835–1842. doi:10.1016/j.ajpath.2012.01.033.
- [32] ssniff® experimental diets for laboratory animals, viewed 2015-04-29.
URL http://www.ssniff.de/documents/gereinigte_diaeten_experimentaldiaeten.pdf
- [33] M. Schwier, T. Böhrer, H. K. Hahn, U. Dahmen, O. Dirsch, Registration of histological whole slide images guided by vessel structures, *Journal of Pathology Informatics* 4 (2013) 10. doi:10.4103/2153-3539.109868.
- [34] C. Broit, Optimal registration of deformed images, Ph.D. thesis, University of Pennsylvania (1981).
URL <http://repository.upenn.edu/dissertations/AAI8207933/>
- [35] E. Haber, J. Modersitzki, Intensity gradient based registration and fusion of multi-modal images, in: C. Barillot, D. R. Haynor, P. Hellier (Eds.), *Medical Image Computing and Computer-Assisted Intervention – MICCAI 2006*, Vol. 3216 of Springer Lecture Notes in Computer Science, 2006, pp. 591–598. doi:10.1007/11866763_89.
- [36] J. Modersitzki, *FAIR: Flexible Algorithms for Image Registration*, SIAM, Philadelphia, 2009.
- [37] S. Hoehme, M. Brulport, A. Bauer, E. Bedawy, W. Schormann, M. Hermes, V. Puppe, R. Gebhardt, S. Zellmer, M. Schwarz, E. Bockamp, T. Timmel, J. G. Hengstler, D. Drasdo, Prediction and validation of cell alignment along microvessels as order principle to restore tissue architecture in liver regeneration, *Proceedings of the National Academy of Sciences of the United States of America* 107 (23) (2010) 10371–10376, supporting Information. doi:10.1073/pnas.0909374107.
- [38] H. Marsman, T. Matsushita, R. Dierkhising, W. Kremers, C. Rosen, L. Burgart, S. L. Nyberg, Assessment of donor liver steatosis: pathologist or automated software?, *Human Pathology* 35 (4) (2004) 430–435. doi:10.1016/j.humpath.2003.10.029.
- [39] M. Selzner, P.-A. Clavien, Fatty liver in liver transplantation and surgery, *Seminars in Liver Disease* 21 (1) (2001) 105–113. doi:10.1055/s-2001-12933.
- [40] A. Homeyer, A. Schenk, J. Arlt, U. Dahmen, O. Dirsch, H. K. Hahn, Practical quantification of necrosis in histological whole-slide images, *Computerized Medical Imaging and Graphics* 37 (4) (2013) 313–322. doi:10.1016/j.compmedimag.2013.05.002.
- [41] F. Aurenhammer, Voronoi diagrams – a survey of a fundamental geometric data structure, *ACM Computing Surveys* 23 (3) (1991) 345–405. doi:10.1145/116873.116880.
- [42] H. K. Hahn, H.-O. Peitgen, IWT – interactive watershed transform: a hierarchical method for efficient interactive and automated segmentation of multidimensional gray-scale images, in: M. Sonka, J. M. Fitzpatrick (Eds.), *Medical Imaging 2003*, Vol. 5032 of Proceedings of SPIE, 2003, pp. 643–653. doi:10.1117/12.481097.
- [43] J. L. Bem, R. Peck, Dextromethorphan, *Drug Safety* 7 (3) (1992) 190–199. doi:10.2165/00002018-199207030-00004.

- [44] A.-M. Yu, R. L. Haining, Expression, purification, and characterization of mouse CYP2d22, *Drug Metabolism and Disposition* 34 (7) (2006) 1167–1174. doi:10.1124/dmd.105.008870.
- [45] N. Blume, J. Leonard, Z. J. Xu, O. Watanabe, H. Remotti, J. Fishman, Characterization of Cyp2d22, a novel cytochrome P450 expressed in mouse mammary cells, *Archives of Biochemistry and Biophysics* 381 (2) (2000) 191–204. doi:10.1006/abbi.2000.1978.
- [46] C. Thiel, S. Schneckener, M. Krauss, A. Ghallab, U. Hofmann, T. Kanacher, S. Zellmer, R. Gebhardt, J. G. Hengstler, L. Kuepfer, A systematic evaluation of the use of physiologically based pharmacokinetic modeling for cross-species extrapolation, *Journal of Pharmaceutical Sciences* 104 (2014) 191–206. doi:10.1002/jps.24214.
- [47] S. Willmann, K. Thelen, J. Lippert, Integration of dissolution into physiologically-based pharmacokinetic models III: PK-Sim[®], *Journal of Pharmacy and Pharmacology* 64 (7) (2012) 997–1007. doi:10.1111/j.2042-7158.2012.01534.x.
- [48] L. O. Schwen, W. Wei, F. Gremse, J. Ehling, L. Wang, U. Dahmen, T. Preusser, Algorithmically generated rodent hepatic vascular trees in arbitrary detail, *Journal of Theoretical Biology* 365 (2015) 289–300. doi:10.1016/j.jtbi.2014.10.026.
- [49] A. Homeyer, A. Schenk, J. Arlt, U. Dahmen, O. Dirsch, H. K. Hahn, Fast and accurate identification of fat droplets in histological images, *Computer Methods and Programs in Biomedicine* 121 (2) (2015) 59–65. doi:10.1016/j.cmpb.2015.05.009.
- [50] H.-G. Holzhütter, D. Drasdo, T. Preusser, J. Lippert, A. M. Henney, The virtual liver: A multidisciplinary, multi-level challenge for systems biology, *Wiley Interdisciplinary Reviews: Systems Biology and Medicine* 4 (3) (2012) 221–235. doi:10.1002/wsbm.1158.
- [51] D. Drasdo, J. Bode, U. Dahmen, O. Dirsch, S. Dooley, R. Gebhardt, A. Ghallab, P. Godoy, D. Häussinger, S. Hammad, S. Hoehme, H.-G. Holzhütter, U. Klingmüller, L. Kuepfer, J. Timmer, M. Zerial, J. G. Hengstler, The virtual liver: state of the art and future perspectives, *Archives of Toxicology* 88 (12) (2014) 2071–2075. doi:10.1007/s00204-014-1384-6.